Rogowski and D-Dot Sensors for Nanosecond High-Voltage and High-Current Pulse Measurements in Impedance-Matched Pulse Generators

Rogowski and D-Dot Sensors for Nanosecond High-Voltage and High-Current Pulse Measurements in Impedance-Matched Pulse Generators

J. J. van Oorschot, *Graduate Student Member, IEEE*, and T. Huiskamp, *Member, IEEE*

***Abstract*— To measure the output voltage and current in our impedance-matched solid-state Marx generator we developed a voltage and current sensor integrated with the IMG structure. One of the advantages of our IMG structure is the coaxial inner transmission line (TL). The end of this TL is the output connection, which consists of a grounded ring and a smaller high-voltage (HV) inner conductor (coaxial). This structure is ideal for fitting D-dot and Rogowski-coil sensors, as these sensors can benefit from the strictly defined electric and magnetic fields in this waveguide. We developed D-dot and Rogowski-coil sensors on printed circuit boards (PCB) and show their usability in our application for measuring HV pulses. The sensors have a bandwidth of about 200 MHz, measure voltages up to 20 kV, and currents up to hundreds of amperes. Their simple PCB design makes them easily reproducible and cheap compared to commercial sensors. Although designed for our IMG, they can be fit on any coaxial line. Next, we made passive integrators to partly integrate the differentiated sensor signal, which improves the signal quality when measured with an oscilloscope. Finally, after software signal postprocessing, we achieve far better voltage measurements and similar current measurements compared to commercial probes.**

***Index Terms*— Current measurement, high-voltage (HV) techniques, Marx generators, pulse measurements, pulse power systems, voltage measurement.**

I. Introduction

KEY factor in pulsed power systems is the ability to measure the produced voltage and current waveforms. Commercial voltage and current sensors are often not suited for the fast rise time pulses in noisy environments or cannot always be easily fit in the sometimes very compact and/or complex structures of high-voltage (HV) pulse generators. Many researchers have developed their own sensors, tailored to specific HV pulse sources. These sensors can be of a simple structure, high bandwidth, and cheap [2], [3], [4], [5], [6], [7], [8].

Recently, we developed a solid-state impedance-matched Marx generator (IMG) based on a transmission-line structure and implemented it with MOSFET switches. The concept of a first prototype was presented in [1], and in the meantime, an improved IMG was developed in Eindhoven and is now able to generate 20-kV pulses. This generator will be used to generate plasma to create plasma-activated water (PAW) [9], [10]. With reaching higher voltages while keeping short rise times (about 5 ns), the need arises for better voltage and current measurement systems. Eventually, these voltage and current measurements will be used to calculate the delivered energy to the application, which will usually be a plasma reactor.

Existing commercial or homemade sensors are either not suited for the output voltage and current requirements or not a good physical fit for this generator. In this article, we will show the design and results of homemade voltage (D-dot) and current (Rogowski) sensors for the IMG, but suitable for any pulse source with a coaxial output connection. These sensors are made on a printed circuit board (PCB), which makes them easily reproduced and cheap. The whole measurement system is discussed, from the sensors to the developed hardware integrator and software correction.

A. Paper Organization

In Section II, we set the requirements and goals for the sensors and explain our measurement method. Then we show the design, the theoretical calculations, the simulations, the actual implementation, and experimental verification of our D-dot voltage sensor and Rogowski current sensor in Sections III and IV, respectively. Next, a hardware integrator circuit is developed to passively integrate (part of) the differentiated signals. This integrator reduces noise and improves the overall recovered waveform and is presented in Section V. Finally, Section VI shows the results of recovering the original signal in software, and Section VII draws the conclusions.

II. System Setup and Sensor Requirements

A. Marx Generator

The IMG consists of a number of stages (1–20), where each stage switches 1 kV and several hundred *A*. Each stage consists of HV capacitors and six 1200-V SiC MOSFETs, combined with diodes (for bypassing the stage). A coaxial transmission line (TL) in the center of the stage connects the stages and delivers the output pulse to the load. It consists of a solid rod as an inner conductor, and brass rings between each

Manuscript received 11 October 2022; revised 22 December 2022 and 6 February 2023; accepted 13 March 2023. Date of publication 29 March 2023; date of current version 21 April 2023. This work was supported by the Dutch Research Organisation Nederlandse Organisatie voor Wetenschappelijk Onderzoek (NWO) under Grant 17183. The review of this article was arranged by Senior Editor R. P. Joshi. *(Corresponding author: J. J. van Oorschot.)*

The authors are with the Electrical Energy Systems Group, Department of Electrical Engineering, Eindhoven University of Technology, 5600 MB Eindhoven, The Netherlands (e-mail: j.j.v.oorschot@tue.nl; t.huiskamp@tue.nl).

Color versions of one or more figures in this article are available at https://doi.org/10.1109/TPS.2023.3259643.

Digital Object Identifier 10.1109/TPS.2023.3259643

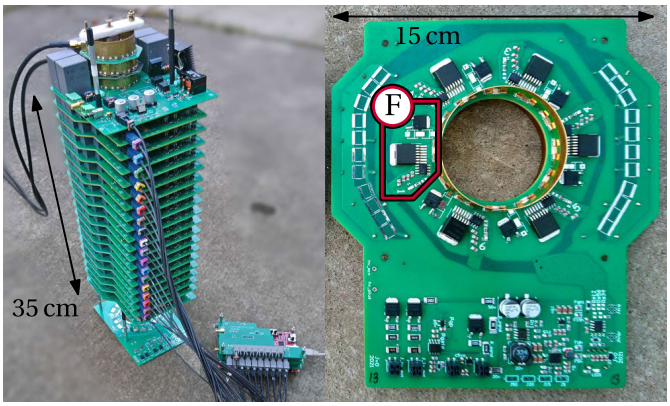

Fig. 1. Left: an IMG of 18 stages, including the final sensors at the coaxial output connection on top and control system at the bottom right. Right: one IMG stage; top view with six switch modules of a MOSFET and diode (one module marked "F"). In the center, the TL outer ring can be seen. The other side of the PCB houses capacitors for HV energy storage.

stage. The brass rings are connected to the stages using metal clips. The generator and a close-up of one stage are shown in Fig. 1. A generic overview of our IMG structure can be found in [1] and detailed information on this generator in [11].

Stages can be switched individually, in which case the not-switched stages will be bypassed by diodes on the stage. This allows for the generation of arbitrary HV waveforms, which we use for plasma research. For instance, it is possible to start the discharge with a short HV pulse and then stop it. A second pulse just after the first one can reignite the plasma, which can have beneficial effects on the chemistry in the plasma [12]. Next to flexible pulses, we can fire each stage at exactly the same time for a short rise time pulse, resulting in about 5-ns rise time for a 10-kV 100-A pulse. The coaxial TL connecting the stages provides a low-inductance path from the stages to the load, preserving the pulse shape of the stage to the load. This feature is the main advantage of the IMG structure and indispensable to generate a short rise time pulse at the output [1], especially when the pulse source becomes physically large compared to the rise time from the switch modules.

B. Sensor Placement

The sensors should be integrated into the TL without disturbing the structure to maintain the pulse form integrity. Most commercial sensors, like a current transformer (CT; e.g., Bergoz/Magnelab [13] or Pearson current probe), or HV probe (e.g., Northstar probe [14]) would need more space than available in the TL structure (while maintaining proper HV isolation), therefore gaps or wider parts of the TL are required, creating discontinuities in the structure. By keeping the sensors physically small, the bandwidth can be high (because of low parasitic inductance and/or capacitance). By integrating sensors in our generator, any load can be connected while keeping the same sensors. This is advantageous for reproducibility (the same sensors are always used and are at the same place in the system) and makes it easy to change the experimental setup as no separate probes have to be connected. Also, if a cable is connected between the generator and load, reflections at the load side will be visible at the generator side, improving energy measurements [5]. Finally, as coaxial geometry is often used, these sensors can be used in any similar system, like an solid-state linear-transformer-driver (SS-LTD) pulse generator [15].

C. Sensor Requirements

First, the sensors should fit in the TL, while not being too close to the inner conductor, as that might cause flashovers from the inner HV conductor to the sensor. The outer diameter of the TL is fixed for our generator at 54 mm. The diameter of the inner HV conductor can be changed, to change the characteristic impedance of the TL and impedance match the generator to a load or cable. At this moment, the output impedance of the generator is set at 50 Ω, which results in a 22-mm inner conductor diameter at the output of the generator.

Second, the bandwidth and gain of the sensors have to be high enough. The wide range of output pulses of our generator sets this requirement. The pulse duration ranges from 30 ns to about 10 μs. Because of the arbitrary output waveforms, voltages down to 1 kV (one-stage switching) and pulses with a long rise time should be measurable as well by our system. In general, voltages from 1 up to 20 kV and currents from 1 up to 500 A should be measurable.

A common rule of thumb for the frequency range of a pulse with a given rise time is given as (0.35/risetime). The fastest pulse rise time observed with this generator is about 3 ns, setting the upper limit to the bandwidth to at least 117 MHz. In plasma processes, higher frequencies can occur as plasma is a complex load, so a higher bandwidth is preferred. Finally, the voltage amplitude has to be high enough for the oscilloscope to measure accurately: A higher gain will reduce the influence of oscilloscope noise and electromagnetic interference (EMI) influence.

D. DI System

The developed sensors will mostly operate in the differentiating regime, producing a differentiated version of the measured signal and therefore the output of the sensors needs to be integrated to reconstruct the waveform. As such, the sensor is part of a differentiating-integrating (DI) measurement system. Previous work [3], [5], [7] shows good results with differentiating sensors to measure voltage and current in pulsed power systems into the GHz range. Another advantage of differentiating sensors is their inherent noise reduction because the differentiated signals are integrated, the noise is also integrated and therefore reduced by a factor of $1/f$ [16], [17].

Fig. 2 shows the frequency response of various components in a DI system. Starting with the sensor in blue, the lower frequency bound is set by f_{meas}, the frequency where the gain becomes too low to measure. Between f_{meas} and $f_{d,\text{sensor}}$, the sensor is fully differentiating. Between $f_{d,\text{sensor}}$ and f_{BW}, parasitic capacitances (in the case of the D-dot sensor) or inductances (in the case of the Rogowski coil) in the sensor housing or cable will integrate the sensor signal, making the sensor self-integrating. Finally, above f_{BW}, the sensor becomes unstable as other parasitic effects become dominant, or the physical sensor size approaches half the signal wavelength.

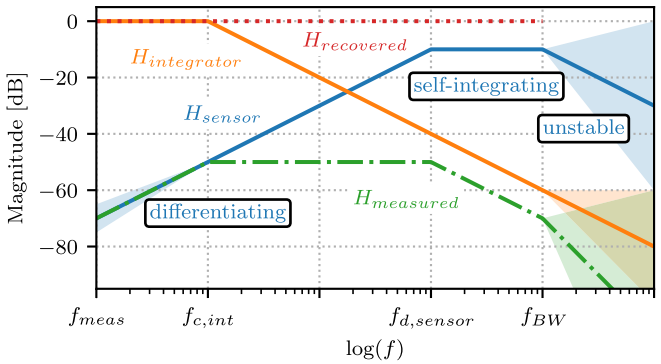

Fig. 2. DI system schematic frequency transfer functions. Shown are the sensor and integrator transfer functions. Three regimes of the sensor are indicated: Differentiating up to $f_{d,\text{sensor}}$, self-integrating (between $f_{d,\text{sensor}}$ and f_{BW}), and unstable (above f_{BW}). Next, the combined frequency response of the sensor and integrator is shown as H_{measured}, with a flat response between $f_{c,\text{int}}$ to $f_{d,\text{sensor}}$. Finally, software correction is used to correct the lower frequency response, resulting in a recovered signal $H_{\text{recovered}}$. This process is further described in Section VI and shown schematically in Fig. 15.

To recover the original waveform (to have a flat frequency response), multiple options are available: First, the sensor can be used in its self-integrating regime; this is how a commercial CT usually operates. Another option is to use the sensor only differentiating and use an integrator to integrate the signal. The integrator response is shown in orange, resulting in an overall measured signal H_{measured} in dash-dotted green, which is flat from $f_{c,\text{int}}$ to $f_{d,\text{sensor}}$. To increase the usable bandwidth (frequency range), both the differentiating and the self-integrating regime of the sensor can be used, as shown in [5]. For this, we measure the transfer function of the sensor using a network analyzer (VNA) and use this to recover the original signal, shown as the dotted red line $H_{\text{recovered}}$. In this work, we use a combination of all techniques: (passive) integrators to integrate the higher frequencies and software recovery to integrate the lower frequencies.

E. Used Equipment and Method for Sensor Characterization

To obtain the transfer function of our sensors, a small part of the 50-Ω IMG TL with the sensors (without switching stages, but with the same geometry) is connected to an Agilent E5061B 5 Hz–3 GHz VNA. The TL is excited by the VNA, as it would usually be from the IMG, and the sensor response is measured as $S21$.

The TL itself is not a perfect waveguide and is not fully closed as can be seen in Fig. 1. We measured the transmission and reflection ($S21$ and $S11$) of the TL, and we concluded that this method of measuring the sensor response performs well up to 200 MHz and reasonably well (to within −3 dB) up to 1 GHz.

III. Voltage Measurement: D-Dot

Voltage measurement is the most important for our generator, as commercial HV probes are of too low bandwidth. In this section, we will present the design consideration, the theoretical calculations, the 3-D electromagnetic (3D-EM) simulations, and the actual implementation and experimental verification of our developed voltage sensor: the D-dot sensor.

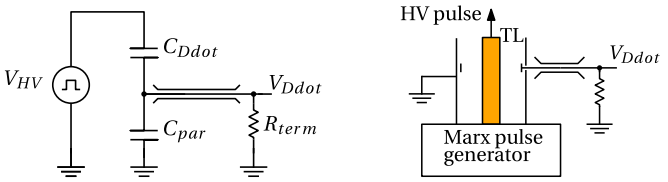

Fig. 3. D-dot sensor equivalent circuit (left) and schematic drawing (right). C_{Ddot} represents the capacitive coupling between the sensor and HV conductor, while C_{par} is the capacitance from the sensor to the ground. The sensor connects via coaxial cable to the output V_{Ddot} with termination resistor R_{term} of 50 Ω.

Fig. 4. D-dot simulated in CST: shown are three TLs of a grounded outside with the HV rod in the center. Around the center are different shapes of the sensor. The sensor is connected to a coaxial cable on the right side. From left to right: interrupted ring, half ring, and arc. Not shown are a full ring and a pin (the pin electrode is just the pin without any ring shape attached).

A. Dimensions and Geometry

For pulse measurements, a capacitive sensor (usually called D-dot or V-dot) has shown very good results and will therefore be used. The sensor acts as a capacitive divider between the output HV and the ground, connected to an oscilloscope using a 50 Ω coaxial cable. The equivalent circuit is shown in Fig. 3.

This D-dot sensor can be made from a small pin (for instance, the pin of a commercial SMA or n-type connector as in [7]) pointing in the TL. Such sensors have been used integrated into coaxial cables [5], [7], but as our TL is larger and the to-be-measured frequencies lower, just a pin electrode will not have enough gain and we will use a larger sensor. Making the sensor electrode larger is possible in three directions: width (going around the TL in a circular shape), height (toward the generator or load side of the TL), and radius (distance to the HV inner conductor). All of these options are indicated in Fig. 4 and will be explained and explored in the next subsections.

B. Theoretical Approach

First, we calculate the sensor response theoretically. Assuming a full ring sensor of a certain height around the HV inner conductor, we can estimate the capacitance (C) of a cylindrical structure using the following equation:

$$C = \frac{2\pi\epsilon_r\epsilon_0}{\ln(r_{\text{outer}}/r_{\text{inner}})} \cdot \text{height}\,;\ \epsilon_r = 1. \tag{1}$$

This estimation neglects all edge effects, so this capacitance will be a lower-bound value. We calculate both C_{Ddot} and C_{par} using this formula, using the inner HV conductor radius, sensor ring radius, and outer TL radius as r_{inner} and r_{outer}, with air in between ($\epsilon_r = 1$). For a D-dot ring-shaped sensor with a 24-mm radius and 1.6-mm height (representative for our IMG system), this gives a C_{Ddot} of 114 fF.

The sensor voltage can now be defined as a capacitive-resistive divider, with C_{Ddot} as the high side of the divider and a parallel connection of C_{par} and R_{term} as the lower part. For

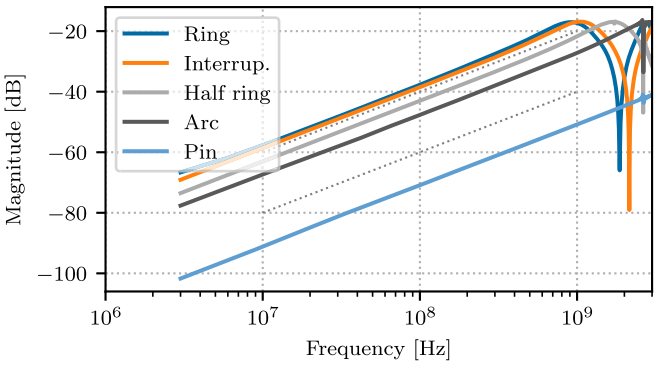

Fig. 5. Simulated transfer function of the D-dot sensor for the pin-to-ring shape variation. Shown are the full ring, three different arcs (see Fig. 4), and the pin. Height = 1.6 mm and radius = 24 mm. A larger sensor has a higher gain, but lower bandwidth.

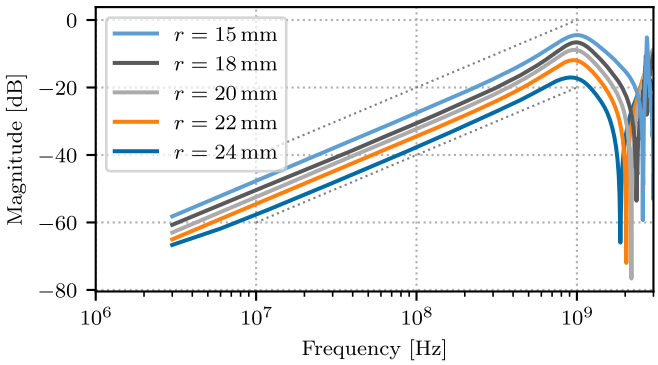

Fig. 6. Simulated transfer function of the D-dot sensor for the radius variation for a full ring sensor of 1.6-mm height. A smaller radius sensor has a stronger resonant peak at about 1 GHz.

the differentiating regime, C_{par} can be neglected in the lower part, as R_{term} is the significant term in the parallel connection. The sensor transfer function H_{Ddot} with $R_{\text{term}} = 50\ \Omega$ is now defined as

$$H_{\text{Ddot}}(j\omega) = \frac{V_{\text{Ddot}}}{V_{\text{HV}}} = \frac{R_{\text{term}}}{Z_{C_{\text{Ddot}}} + R_{\text{term}}} \approx j\omega C_{\text{Ddot}} R_{\text{term}}. \quad (2)$$

When including the parallel capacitance to ground C_{par}, the transfer becomes

$$H_{\text{Ddot}}(j\omega) = \frac{V_{\text{Ddot}}}{V_{\text{HV}}} = \frac{j\omega C_{\text{Ddot}} R_{\text{term}}}{1 + j\omega R_{\text{term}}(C_{\text{Ddot}} + C_{\text{par}})}. \quad (3)$$

This estimated gain results in around a 10-V peak for a typical 10-kV pulse from the IMG, which is enough to recover the original waveform.

C. 3D-EM Simulation

Now that we know that the form factor of a ring has enough gain, 3D-EM simulations are performed using CST Studio Suite 2020 [18] (CST). A 3-D model of the sensor is excited using a waveguide port in a time-domain simulation to gain more insights into gain and bandwidth considerations for different sensor sizes (width, height, and radius).

We start with the sensor width. Fig. 4 shows some options for increasing the width by going around the inner conductor as a ring shape. The simulation results are shown in Fig. 5, showing that the smaller sensors have higher bandwidth at the cost of a lower gain. This can be explained by the capacitances in the sensor: a small sensor has a small C_{Ddot} and C_{par}. A small C_{Ddot} results in a lower gain and a lower C_{par} results in a higher bandwidth. For larger sensors, the opposite holds.

Next, we vary the sensor radius (r in Fig. 4), assuming a ring-shaped sensor. This is shown in Fig. 6.

As expected, the sensor gives some resonance at higher frequencies because of the physical size of the sensor (both because of the travel time of the signal around the sensor and because of inductance). Especially, the smaller-radius sensors show a resonant peak around 1 GHz. This is explained by the parasitic inductance of the wire running from the sensor toward the TL wall, to the coaxial cable. After 1 GHz, the parasitic effects become dominant and a resonant valley is formed. This is visible at around 2 GHz for the ring shape sensor of 24-mm radius and can be explained by the signal propagation through the sensor electrode. A signal picked up at the far side of the ring (away from the cable) results in a signal travel time of $\pi r/c = 250$ ps in air, which is exactly the half-period time of a 2-GHz signal (this effect is also shown in [8]). While the smaller radius increases the gain (without much penalty in the bandwidth) as the capacitive coupling increases, the risk of HV flashover from the inner conductor to the sensor also increases, so this solution might not be practical.

Finally, the height of the sensor (h in Fig. 4) was varied from 1 to 10 mm. A higher sensor (from a ring to a cylindrical shape) has a higher gain. Parasitic effects did not seem to change by changing the height, therefore this result is not shown.

D. Implemented D-Dot Sensor

Until now, we assumed a floating ring inside the TL, but this is not mechanically stable. Therefore, we chose to make the D-dot sensor on a PCB, as an edge-plated ring. The sensor height is set to a standard PCB thickness of 1.6 mm, allowing for commercial production by multiple manufacturers. We opted for the largest diameter design (24 mm) because of HV isolation to the inner TL. To compensate for its low gain compared to smaller diameters, the full-ring design is chosen. An additional advantage of the full ring shape sensor is the low sensitivity for a not exactly centered center (HV) conductor in the TL. Making the sensor this way reduces costs (only a few euros for PCB manufacturing), integrates into the TL like any of the Marx stages, and is easily reproduced if more D-dot sensors are needed. The resulting sensor is shown in Fig. 7.

A new simulation was performed in CST, this time including the PCB between the sensor and grounded outside, because the capacitance to ground C_{par} will increase due to the higher permittivity of the PCB material. This simulation, together with a VNA calibration measurement and the fit transfer function, is shown in Fig. 8. The transfer functions (2) and (3) with $R_{\text{term}} = 50\ \Omega$ were fit using SciPy "optimize.curve_fit" [19] on the measured response, and C_{Ddot} was determined to be 340 fF and C_{par} of 14.4 pF. As expected, the capacitances are

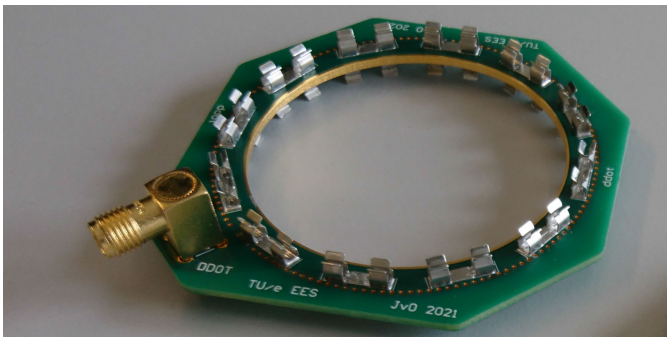

Fig. 7. D-dot sensor implemented as an edge-plated ring on a PCB, connected to an SMA connector. Metal clips connect to the outer (gnd) conductor of the IMG TL.

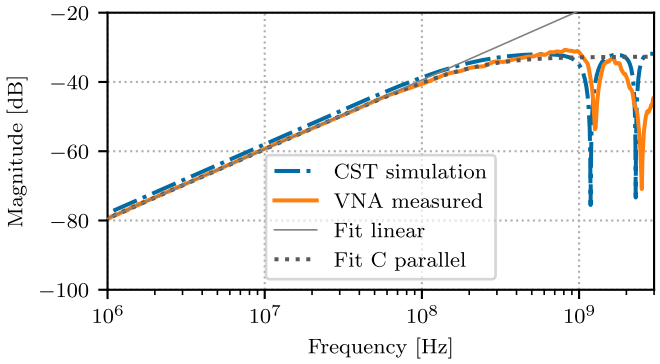

Fig. 8. D-dot frequency response: 3D-EM simulated (CST) and measured with VNA. Fit curves for linear fit as (2) and fit with parallel C_{par} as in (3) on the measured data. The response is stable up to 1 GHz after which two resonant valleys follow.

higher than calculated in Section III-B due to edge effects. The CST simulations and measurements match up nicely. The first resonant valley now is at 1.25 GHz (instead of 2 GHz in Fig. 6), which is also the result of the FR-4 PCB material (signals travel slower through higher ϵ material). A second valley is found at the double frequency of 2.5 GHz.

The sensor upper bandwidth is determined to be 1 GHz, after which instabilities occur. Recovery of the signal with the fit transfer function is possible up to 330 MHz, after which the fit response deviates more than 1% from the measured response. Concluding, we have developed a PCB-based D-dot sensor with higher bandwidth than commercial HV probes at a fraction of the costs.

IV. Current Measurement: Rogowski

Developing a new measurement system for the current in our IMG is less critical than for the voltage, as commercial CTs perform well up to a few 100 MHz. Still, a CT is difficult to fit in the TL, as the sensor needs enough clearance from the center HV conductor and the outer conductor should not be interrupted too much. Current measurement can be performed with an inductively coupled sensor, either with a single inductive loop (usually called B-dot) [5] or with multiple loops as a Rogowski-coil [20]. The schematic of the inductive sensors is shown in Fig. 9.

Another option to measure current is using a shunt resistor on the return wire, like in [6]. Such a structure is sensitive to

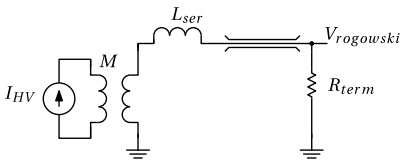

Fig. 9. Rogowski circuit: indicated are the mutual coupling or gain M from the high current I_{HV} to the sensor output V_{rogowski} and a termination resistor of 50 Ω. The sensor has some parasitic inductance L_{ser} limiting the usable bandwidth.

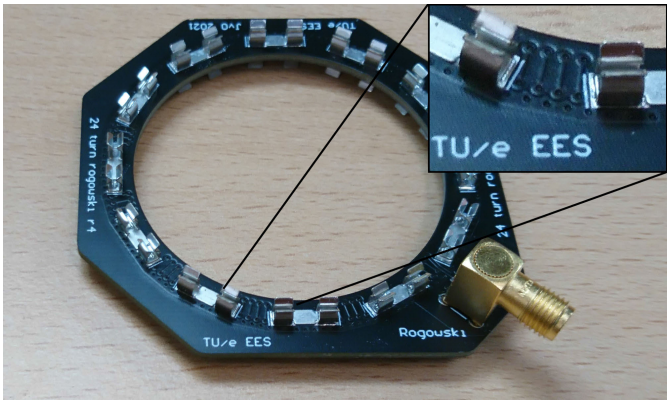

Fig. 10. Rogowski implemented design, version 4-NS. This version of the sensor has four turns between the first six metal clips.

noise and special care has to be taken to prevent ground loops as the shunt creates a floating ground.

Initially, we made a design for a single-loop B-dot sensor, but the gain was too low and too much parasitic effects occurred for accurate measurements. Instead, we developed a Rogowski coil on PCB [21], [22], [23], [24]. Numerical simulation of this structure is complex [22] so was not performed; instead, some different designs were manufactured and are compared in this section.

A. Dimensions and Geometry

The Rogowski coil is constructed on a PCB and connects to the outer TL brass rings with metal clips, in the same way as the stages and the D-dot sensor. The turns of the Rogowski sensor are made from traces on two layers, connected with vias, and placed in between the metal clips, as shown in Fig. 10. This way the limited space is used optimal while maintaining the isolation distance to the HV conductor. The PCB bottom and top clips (both ground) are connected with vias (from top to bottom layer) in a ring shape just outside the clips. This way, all IMG output return current must flow through the vias, around the Rogowski turns. Initially, two turns are placed between each clip, resulting in 24 windings.

We decided to place the turns of the Rogowski on the first and third layers on a four-layer PCB and the return wire on the second layer. For the loop-trace layout, we use the fish-bone layout as suggested in [23] for noise immunity. An optional E-field shield can be placed on the fourth layer, clarified in Table I and Fig. 11. Such a shield can help for noise immunity and to limit capacitive coupling to the HV electrode (parasitic D-dot effect) [24]. Most of the noise is expected to come from the generator side, therefore the first layer (with loop traces) is

TABLE I
PCB LAYERS IN THE ROGOWSKI DESIGNS

Layer	Position	Function
l1 (red)	Top layer	clips; top part of loop
l2 (brown)	Top inner	return wire through turns
l3 (cyan)	Bottom inner	bottom part of loop
l4 (blue)	Bottom layer	clips; possible e-field shield

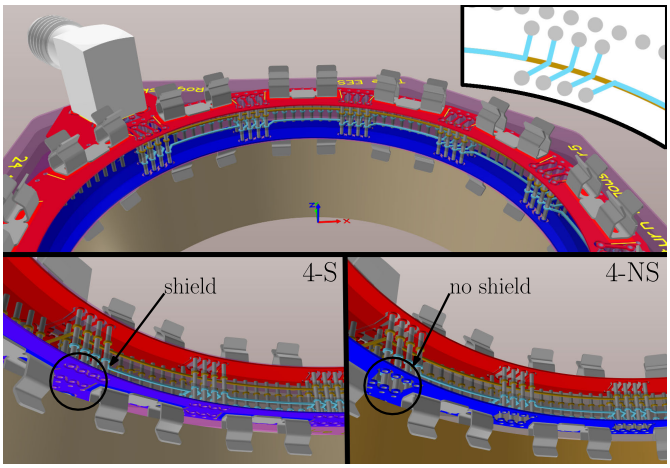

Fig. 11. Three-dimensional view of the Rogowski PCB design, with four turns between the clips. The layer spacing is increased for visibility. Layers as in Table I. Top: the PCB from the top with the SMA connector. Bottom left: design 4-S with the shield and bottom right: design 4-NS without the shield.

placed away from the generator and the fourth layer (with an optional shield) faces the generator. Versions with and without a shield on the fourth layer are designed and the difference is measured. Unfortunately, the shield also couples capacitively to the Rogowski traces, limiting the bandwidth, which will be shown in the following sections. Six or more layer PCBs could be advantageous for more shielding layers but are not considered, as this will also generate more capacitive coupling, limiting the bandwidth.

B. Theoretical Approach

The expected sensor voltage is derived using Faraday's law

$$V_{\text{Rogowski}} = -N\mu_0\mu_r \iint_S \frac{\partial \vec{H}}{\partial t} d\vec{S} = -N\frac{\mu_0\mu_r}{2\pi}\frac{\partial I_{\text{HV}}}{\partial t}\iint_S \frac{h}{r} d\vec{S} \tag{4}$$

where r and h are, respectively, the radius and height of a sensor loop, covering area S, and N is the number of turns. The integral is solved as (rewriting $(\partial/\partial t)$ to $j\omega$)

$$V_{\text{Rog.}} = -I_{\text{HV}} j\omega N \frac{\mu_0\mu_r h}{2\pi}\left(\ln|r_1| - \ln|r_2|\right). \tag{5}$$

This is written as a transfer function as

$$H_{\text{Rog.}}(j\omega) = \frac{V_{\text{Rog.}}}{I_{\text{HV}}} = j\omega M \tag{6}$$

with $r_1 = 27.7$ mm, $r_2 = 25.5$ mm as the loop radius measured from the TL center, and $h = 1.4$ mm, from which we get $M = 5.56 \cdot 10^{-10}$ ($N = 24$ and $\mu_r = 1$).

TABLE II
ROGOWSKI DESIGNS, FIT VALUES, AND USABLE BANDWIDTH

Name	#Turns	Shield	Fit. Gain M	Fit. L_{ser}	BW (1% fit.)
2-S	$12 \cdot 2$	yes	$4.89{\cdot}10^{-10}$	165 nH	45 MHz
2-NS	$12 \cdot 2$	no	$4.57{\cdot}10^{-10}$	177 nH	64 MHz
4-S	$6 \cdot 4$	yes	$4.09{\cdot}10^{-10}$	97 nH	127 MHz
4-NS	$6 \cdot 4$	no	$3.87{\cdot}10^{-10}$	105 nH	129 MHz

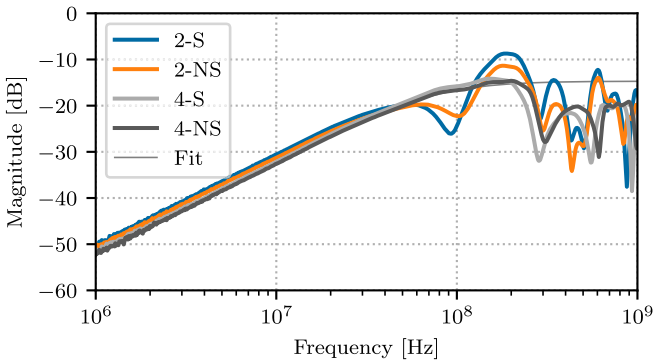

Fig. 12. Rogowski frequency response as measured with VNA for four different designs. A fit line from (7) is shown for design 4-NS, the fit values are shown in Table II. The designs 4-S/NS have a significantly higher bandwidth than 2-S/NS, and the NS-versions have a slightly higher bandwidth than S-versions.

This estimated gain results in around 30-V peak for a typical 200-A pulse from the IMG, which is enough to recover the original waveform.

When taking the parasitic effects into account, the transfer function becomes

$$H_{\text{Rog.}}(j\omega) = \frac{j\omega M}{1 + j\omega L_{\text{ser}}/R_{\text{term}}} \tag{7}$$

where L_{ser} combines all parasitic effects into an equivalent series inductance and $R_{\text{term}} = 50\ \Omega$ is the cable termination.

C. Implemented Rogowski Sensor

In total, four different designs were made, all with 24 turns, summarized in Table II. The first two designs have two turns between each clip for 12 clips and the second two designs have four turns between six clips (covering only half the circle). Both have the same number of turns and therefore a similar gain, but as the four-turn version only covers half the circumference, the parasitic inductance is lower, which increases the bandwidth. A possible disadvantage of the four-loop version on a half circle is that the center conductor, carrying the HV current, should be exactly in the center for a correct measurement.

As a second parameter, we changed whether an E-field shield was placed on the bottom PCB layer. The design is shown in Fig. 11, where the bottom figures show a version with and without the bottom shield placed.

We named the four versions based on turn configuration (2 or 4) and shield (S) or no shield (NS) placed. The designs were built and measured with a VNA. The transfer function (7) with $R_{\text{term}} = 50\ \Omega$ is fit on the measured data using SciPy "optimize.curve_fit" [19] and shown in Fig. 12. The fit values

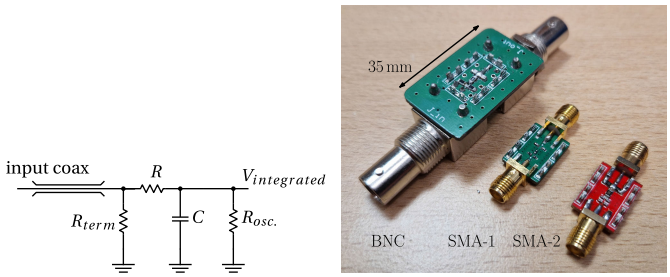

Fig. 13. Integrator circuit (left) and the implemented PCBs (right): showing the BNC type integrator and both SMA-type integrators.

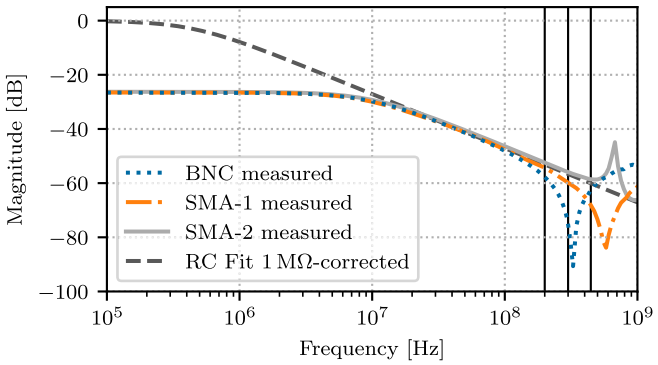

Fig. 14. Measured frequency response of the integrators when connected to a VNA with 50-Ω input impedance. This is used to fit values for R, C, and L_{ser}. The integrator RC transfer function, (8) is shown with these fit values, corrected for a 1-MΩ oscilloscope impedance. Horizontal lines indicate the usable bandwidth of the BNC, SMA-1, and SMA-2 type, respectively.

are summarized in Table II, as well as the bandwidth where the fit functions start to deviate more than 1% from the measured response. The effect of the noise shield on noise was not significant, but the effect of the capacitive coupling is visible in the bandwidth results. Design 4-NS is chosen as the final design as it has the highest bandwidth of 129 MHz and is stable up to 200 MHz.

V. Hardware Integrator

To recover the original waveform from the sensor output, the differentiated signal has to be integrated, as explained in Section II-D. This can be performed using software integration, hardware (passive or active) integration, or a combination. Since we want to use the differentiating and self-integrating regime of our sensors, some recovery in the software will always be needed as the overall response is not flat in this case (see Fig. 2). In this case, a passive hardware integrator can still be advantageous in integrating the highest frequencies of the sensors, reducing high-frequency noise, discarding dc offsets, and using the oscilloscope resolution more effectively (further explained in Section VI-B). Passive hardware integrators are mostly constructed as an RC-low pass filter and can integrate frequencies above the RC cutoff frequency $f_{c,\text{int}} = (RC)^{-1}$ Hz as shown in Fig. 2. To integrate the lower frequencies as well, an active (including amplifier) hardware integrator can be used, but these require more complex circuits [24], [25]. Instead, we integrate the lower frequencies in software, combining the best features of passive hardware integration with the flexibility and ease of software integration. We have developed three designs of an RC passive integrator to be placed between the sensor and oscilloscope.

The following sections will explain our design choices and show the performance of the developed integrators.

A. Theoretical Approach

The developed integrators are passive RC integrators and are shown in Fig. 13. The (RC) transfer function, including the internal oscilloscope impedance $R_{\text{osc.}}$ is

$$H(j\omega) = \frac{R_{\text{osc.}}}{R_{\text{osc.}}(1 + j\omega C) + R}. \tag{8}$$

First, resistor R was set at 1 kΩ, as a tradeoff between signal strength at the oscilloscope, and isolation of the coaxial cable matching from the integration capacitors. Then the capacitor value was chosen as a tradeoff between signal strength and integration bandwidth and came to about 360 pF. This sets the RC time to 360 ns, which is in the timescale of our most common pulse lengths, so the integrator will integrate a large part of the signal.

B. Implemented Passive Integrators

Three different designs were made: a large one with BNC connectors and two smaller ones with SMA connectors (SMA-1 and SMA-2), all with surface mount device (SMD) components, shown in Fig. 13 and summarized in Table III. R_{term} is made out of two 110 Ω 1% resistors in parallel and R is an 1 kΩ 1% resistor. C is made from two 180-pF C0G 5% capacitors in parallel for the BNC and SMA-1 design and from four 82-pF C0G RF capacitors (total 328 pF) in parallel for design SMA-2. These RF capacitors are more suitable for high frequencies.

All integrators are connected to a VNA to measure their S_{21} parameters (the transfer function). This VNA is calibrated at 50 Ω on both ports, setting $R_{\text{osc.}}$ to 50 Ω, while $R_{\text{osc.}}$ will be 1 MΩ for normal measurement operation. Fig. 14 shows the three measured responses (at $R_{\text{osc.}}$ to 50 Ω) and the RC transfer function (8) with $R_{\text{osc.}}$ to 1 MΩ. Next, an RCL transfer function (L_{ser} added to (8) as parasitic series inductance) is fit on the BNC and SMA-1 measured data using SciPy "optimize.curve_fit" [19] to determine the actual R, C, and parasitic L_{ser} of the integrators. SMA-2 has a different oscillation characteristic that cannot be fit using this function, so just (8) is used to determine its R and C. Later on, these functions with fit values are used to recover the original signal for the total system. The fit values, as well as the self-resonance bandwidth and the bandwidth where the fit RC and RCL functions are within 1% of the measured data are shown in Table III.

For the BNC version, the bandwidth is limited by the BNC connector connection inductance, while for the SMA-1 version, the series inductance of the capacitors is dominant. In both cases, this results in a self-resonance frequency of $f_{\text{s.r.}} = (2\pi(LC)^{1/2})^{-1}$, which causes the bandwidth limit of the integrator. For the BNC and SMA-1 integrators, recovery up 311 and 423 MHz is theoretically possible using the RCL

TABLE III
INTEGRATOR DESIGNS, COMPONENTS WITH SMD PACKAGE TYPE, FIT VALUES, AND 1%-FIT BANDWIDTH

Name	R_{term}	R	Fit. R	C	Fit. C	Fit. L_{ser}	$f_{\mathrm{s.r.}}$	$\mathrm{BW_{RC}}$	$\mathrm{BW_{RCL}}$
BNC	2×110 Ω 0805	1 kΩ 0805	1.01 kΩ	2×180 pF C0G 0805	354 pF	700 pH	320 MHz	70.0 MHz	311 MHz
SMA-1	2×110 Ω 0402	1 kΩ 0402	1.01 kΩ	2×180 pF C0G 0402	360 pF	229 pH	554 MHz	111 MHz	423 MHz
SMA-2	2×110 Ω 0805	1 kΩ 0805	9.78 kΩ	4×82 pF C0G RF 0402	336 pF	(not fit.)	675 MHz	445 MHz	(not fit.)

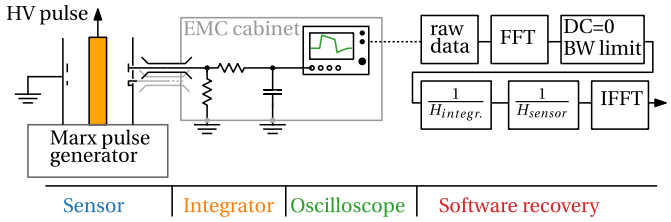

Fig. 15. Schematic representation of the process: IMG with sensors, connected with integrators to the oscilloscope in an EMC cabinet. Stored waveforms are postprocessed in software using the fit sensor and integrator transfer functions to recover the original waveform. Colors correspond to those used in Fig. 2.

fit transfer functions, but near the resonant valley, the signal gets very weak and a lot of noise is to be expected. With keeping some margin from the resonant valley, we set the usable bandwidth for the BNC type to 200 MHz and for the SMA-1 type to 300 MHz. The SMA-2 integrator has RF capacitors that behave differently and generate a resonant peak instead of a valley. Therefore, recovery of the signal using this integrator is possible till 445 MHz using just the fit RC transfer function.

VI. COMPLETE SETUP AND SOFTWARE RECOVERY

As explained in Sections II and V, we want to use both the differentiating and self-integrating regimes of our sensors, possibly combined with passive integrators. Therefore, software correction of the signals is necessary. Fig. 15 shows the full setup schematically: the IMG with coaxial TL output connection on the left, with sensors connected with coaxial cable to feed-through on an electromagnetic compatibility (EMC) cabinet. The cabinet removes common mode current from the ground shield and protects the measuring equipment from electromagnetic radiation from the outside [16]. The passive integrators shown in the previous section are placed on the oscilloscope in the EMC cabinet and the waveforms are saved and processed on a computer. In postprocessing, the stored waveform is converted to the frequency domain using fast Fourier transform (FFT) (Numpy "numpy.fft.rfft" [26]), where any dc component in the signal is removed, and a bandwidth limit can be applied. Next, the inverted fit transfer function of both the sensors (3) and (7) and integrator (8) are multiplied with the frequency-domain signal and the signal is converted back to the time domain using inverse FFT (IFFT) (Numpy "numpy.fft.irfft" [26]). An important detail here is to add the oscilloscope input capacitance (typically 10–20 pF) to the integrator C in the fit transfer function.

Relating to Fig. 2, the green line H_{measured} as stored by the oscilloscope is converted to the red line $H_{\mathrm{recovered}}$ by this postprocessing.

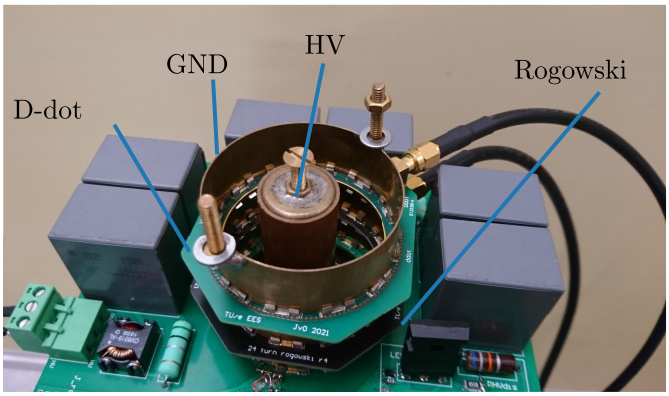

Fig. 16. Top side of the IMG, showing the coaxial output connection of the TL (marked GND and HV). Both the D-dot and Rogowski sensor are connected at the output of the IMG.

A. Calibration

To validate the new measurement system with HV pulses, we measure an output pulse of a ten-stage (10 kV) IMG [11] with our sensors together with commercial probes. Both the D-dot and Rogowski sensors are connected to the IMG output as shown in Fig. 16.

The commercial probes used are a Northstar PVM-1 probe with 90-MHz [14] bandwidth for voltage measurement and a Bergoz/MagneLab [13] CT-B2.5 CT with 500-MHz bandwidth for current measurement. The CT measures the current on the HV output (high side), like the Rogowski sensor. The four resulting waveforms are captured by a LeCroy WaveRunner 620Zi (2 GHz, 10 GSample/s, 8-bit) digital storage oscilloscope. As extra validation, we use a 4-m 50-Ω coaxial cable as load, so our impedance at the beginning of the pulse is very well-defined (a coaxial cable has less parasitic effects than a resistor). This cable is terminated with a 110-Ω resistor, this mismatched load produces reflections, which our sensors should be able to capture. The reflections have different effects on the voltage and current at the generator side, and therefore these can prove that our current and voltage measurements are working independently. Fig. 17 shows the measurement results, together with an LTSpice [27] simulation of the load for reference.

The Northstar results show oscillations, introduced by its physical size and long ground lead (about 20 cm). Because of these oscillations, the small voltage reflection peak at 45 ns is not clearly discernible. The results show that our D-dot sensor is a significant improvement over the Northstar probe for voltage measurement. For the current measurement, the Rogowski and Bergoz sensor perform similarly, but the Bergoz probe appears slower. This might be due to the parasitic effects of the sensor coupling to HV rather than a bandwidth

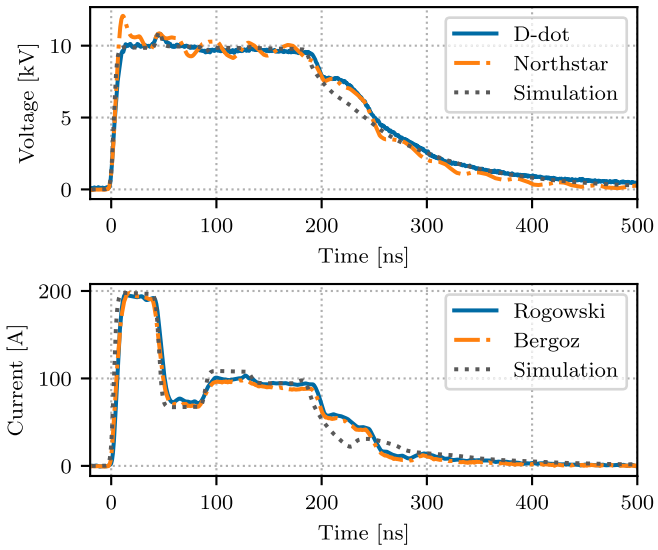

Fig. 17. Voltage and current as expected from simulation, measured with our new system (Rogowski and D-dot) and measured with commercial probes (Northstar PVM-1 and Bergoz CT-B2.5). Note that simulation is not accurate for turn-off behavior, after 200 ns. The new sensors show very good results, especially in voltage measurement.

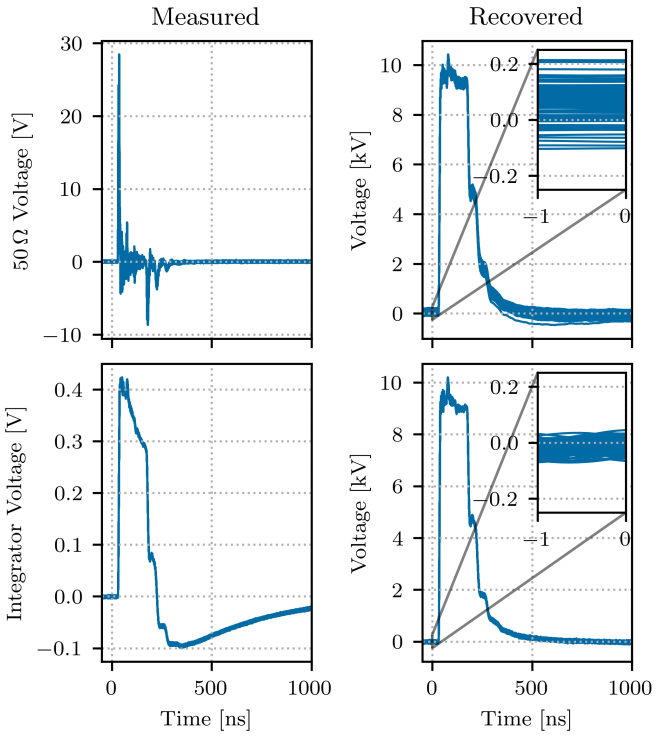

Fig. 18. Hundred measured voltage waveforms as measured with D-dot terminated with 50-Ω (top left) and integrated in software (top right). Using hardware passive integrator (bottom left) and recovered in software (bottom right). The inset in the right side figures shows the overlay of the waveforms just before the pulse starts.

limit. Note that the simulation is not accurate for IMG turn-off behavior, so the simulated waveform is not representative after 200 ns.

Next to these, the sensors were tested with many pulse shapes, all giving accurate results, and some shown in [11]. Of course, the noise will gain more influence for longer pulse lengths and/or lower measured voltages or currents. Measurements on sensor overshoot/undershoot are not taken, as the parasitic effects of the IMG, used HV switches (MOSFETs) and load is dominant here.

B. Effect of Passive Integrator

Until now, we assumed that the integrator would improve the signal quality, which will now be shown by overlaying multiple consecutive measured pulses. The voltage waveform from Fig. 17 is measured 100 times with both a normal 50 Ω termination on the oscilloscope and with a BNC-type integrator. In both cases, the waveforms are postprocessed as shown in Fig. 15, but for the 50-Ω termination, the integrator transfer ($1/H_{\text{integr.}}$) is left out. Even though the signal with 50-Ω termination is much higher (about 30-V peak versus 400-mV peak), the recovered signal has a worse overlay as shown in Fig. 18. This is both explained by the noise filtering in the integrator and the better use of oscilloscope resolution with the integrator (a lower peak-to-average signal is measured). Already before the pulse starts, the overlay of the 50-Ω termination is worse than the passive integrated signals, as shown in the inset figure.

There is one exception to this result: The integrators do need quite some signal, for lower amplitude measurements, the 50-Ω termination performs better as the signal becomes too weak after the integrator is properly measured by the oscilloscope.

VII. Conclusion

In this article, we presented our newly developed D-dot voltage sensor and Rogowski current sensor on PCB, which can be directly attached to the IMG TL output connection. We showed the development process of both sensors, the design choices, and their result on the achieved bandwidth and gain. Next, we showed the development process of a hardware integrator and show how this improves the measured waveforms. Finally, the sensors, combined with passive integrators and software recovery are shown to accurately measure the produced HV waveforms. Currents of hundreds of amperes are recoverable up to 100 MHz and voltages of tens of kV up to 300 MHz with software recovery using a fit transfer function. With a more complex transfer function, the signal can be recovered up to 200 MHz for the current sensors and to 1 GHz for our voltage sensor. The combined system of D-dot and Rogowski sensor with passive integrator results in a measured signal gain of about 400 mV/10 kV and 200 mV/200 A. All goals in terms of bandwidth and gain are reached, with similar or better results than commercial probes.

References

[1] T. Huiskamp and J. J. Van Oorschot, "Fast pulsed power generation with a solid-state impedance-matched Marx generator: Concept, design, and first implementation," *IEEE Trans. Plasma Sci.*, vol. 47, no. 9, pp. 4350–4360, Sep. 2019. [Online]. Available: https://ieeexplore.ieee.org/document/8812678

[2] W. Stygar et al., "D-dot and B-dot monitors for Z-vacuum section power-flow measurements," in *Proc. IEEE Int. Pulsed Power Conf.*, vol. 2, Jun. 1997, pp. 1258–1263. [Online]. Available: https://ieeexplore.ieee.org/document/674573

[3] T. C. Wagoner et al., "Differential-output B-dot and D-dot monitors for current and voltage measurements on a 20-MA, 3-MV pulsed-power accelerator," *Phys. Rev. Special Topics-Accel. Beams*, vol. 11, no. 10, Oct. 2008, Art. no. 100401. [Online]. Available: https://link.aps.org/doi/10.1103/PhysRevSTAB.11.100401

[4] C. A. Ekdahl, "Voltage and current sensors for a high-density Z-pinch experiment," *Rev. Sci. Instrum.*, vol. 51, no. 12, pp. 1645–1648, Dec. 1980. [Online]. Available: https://aip.scitation.org/doi/10.1063/1.1136140

[5] T. Huiskamp, F. J. C. M. Beckers, E. J. M. van Heesch, and A. J. M. Pemen, "B-dot and D-dot sensors for (sub)nanosecond high-voltage and high-current pulse measurements," *IEEE Sensors J.*, vol. 16, no. 10, pp. 3792–3801, May 2016. [Online]. Available: https://ieeexplore.ieee.org/document/7409924

[6] A. Khomenko, V. Podolsky, and X. Wang, "Different approaches of measuring high-voltage nanosecond pulses and power delivery in plasma systems," *Electr. Eng.*, vol. 103, no. 1, pp. 57–66, Feb. 2021, doi: 10.1007/s00202-020-01058-8.

[7] B. M. Novac et al., "Theoretical and experimental studies of off-the-shelf V-dot probes," *IEEE Trans. Plasma Sci.*, vol. 46, no. 8, pp. 2985–2992, Aug. 2018. [Online]. Available: https://ieeexplore.ieee.org/document/8419077

[8] M. R. Ulmaskulov, S. A. Shunailov, K. A. Sharypov, and E. M. Ulmaskulov, "Picosecond high-voltage pulse measurements," *Rev. Sci. Instrum.*, vol. 92, no. 3, Mar. 2021, Art. no. 034701. [Online]. Available: https://aip.scitation.org/doi/10.1063/5.0028419

[9] P. J. Bruggeman et al., "Plasma-liquid interactions: A review and roadmap," *Plasma Sources Sci. Technol.*, vol. 25, no. 5, Sep. 2016, Art. no. 053002. [Online]. Available: https://iopscience.iop.org/article/10.1088/0963-0252/25/5/053002

[10] C. Bradu, K. Kutasi, M. Magureanu, N. Puac, and S. Živkovic, "Reactive nitrogen species in plasma-activated water: Generation, chemistry and application in agriculture," *J. Phys. D: Appl. Phys.*, vol. 53, no. 22, May 2020, Art. no. 223001. [Online]. Available: https://iopscience.iop.org/article/10.1088/1361-6463/ab795a

[11] J. J. van Oorschot and T. Huiskamp, "Fast and flexible, arbitrary waveform, 20-kV, solid-state, impedance-matched Marx generator," *IEEE Trans. Plasma Sci.*, vol. 51, no. 2, pp. 560–571, Feb. 2023. [Online]. Available: https://ieeexplore.ieee.org/document/10021259/

[12] T. Huiskamp, C. Ton, M. Azizi, J. J. van Oorschot, and H. Höft, "Effective streamer discharge control by tailored nanosecond-pulsed high-voltage waveforms," *J. Phys. D: Appl. Phys.*, vol. 55, no. 2, Oct. 2021, Art. no. 024001, doi: 10.1088/1361-6463/ac2969.

[13] *GMW Associates—MagneLab CT Current Transformers—Overview*. Accessed: Mar. 13, 2023. [Online]. Available: https://gmw.com/product/ct/

[14] *High Voltage Probes*. Accessed: Mar. 13, 2023. [Online]. Available: https://www.highvoltageprobes.com

[15] W. Jiang, "Review of solid-state linear transformer driver technology," *Matter Radiat. Extremes*, vol. 3, no. 4, pp. 159–164, Jul. 2018. [Online]. Available: https://aip.scitation.org/doi/10.1016/j.mre.2018.02.001

[16] M. A. Van Houten, E. J. M. Van Heesch, A. P. J. Van Deursen, R. G. Noij, J. N. A. M. Van Rooij, and P. C. T. Van der Laan, "General methods for protection of electronics against interference, tested in high-voltage substations," in *Proc. 8th Int. Symp. Electromagn. Compat.*, 1989, pp. 429–434. [Online]. Available: https://research.tue.nl/en/publications/general-methods-for-protection-of-electronics-against-interferenc

[17] F. Barakou, P. A. A. F. Wouters, S. Mousavi-Gargari, J. P. W. de Jong, and E. F. Steennis, "Online transient measurements of EHV cable system and model validation," *IEEE Trans. Power Del.*, vol. 34, no. 2, pp. 532–541, Apr. 2019. [Online]. Available: https://ieeexplore.ieee.org/document/8492437

[18] *CST Studio Suite*. Accessed: Mar. 13, 2023. [Online]. Available: https://www.cst.com/

[19] *Python SciPy*. Accessed: Mar. 13, 2023. [Online]. Available: https://scipy.org/

[20] W. Rogowski and W. Steinhaus, "Die messung der magnetischen spannung: Messung des linienintegrals der magnetischen feldstärke," *Archiv für Elektrotechnik*, vol. 1, no. 4, pp. 141–150, Apr. 1912. [Online]. Available: http://link.springer.com/10.1007/BF01656479

[21] M. Azizi, J. J. van Oorschot, and T. Huiskamp, "Ultrafast switching of SiC MOSFETs for high-voltage pulsed-power circuits," *IEEE Trans. Plasma Sci.*, vol. 48, no. 12, pp. 4262–4272, Dec. 2020. [Online]. Available: https://ieeexplore.ieee.org/document/9274514

[22] T. Guillod, D. Gerber, J. Biela, and A. Muesing, "Design of a PCB Rogowski coil based on the PEEC method," in *Proc. 7th Intl. Conf. Integr. Power Electron. Syst.*, Mar. 2012, pp. 1–6. [Online]. Available: https://ieeexplore.ieee.org/document/6170681

[23] M. Tsukuda, M. Koga, K. Nakashima, and I. Omura, "Micro PCB Rogowski coil for current monitoring and protection of high voltage power modules," *Microelectron. Rel.*, vol. 64, pp. 479–483, Sep. 2016. [Online]. Available: https://linkinghub.elsevier.com/retrieve/pii/S002627141630155X

[24] L. Ming, Z. Xin, C. Yin, P. C. Loh, and Y. Liu, "Screen-returned PCB Rogowski coil for the switch current measurement of SiC devices," in *Proc. IEEE Appl. Power Electron. Conf. Exposit. (APEC)*, Mar. 2019, pp. 958–964. [Online]. Available: https://ieeexplore.ieee.org/document/8721915

[25] A. P. J. van Deursen, H. W. M. Smulders, and R. A. A. de Graaff, "Differentiating/integrating measurement setup applied to railway environment," *IEEE Trans. Instrum. Meas.*, vol. 55, no. 1, pp. 316–326, Feb. 2006. [Online]. Available: https://ieeexplore.ieee.org/document/1583896

[26] *NumPy*. Accessed: Mar. 13, 2023. [Online]. Available: https://numpy.org

[27] *LTSpice*. Accessed: Mar. 13, 2023. [Online]. Available: https://www.analog.com/en/design-center/design-tools-and-calculators/ltspice-simulator.html

J. J. van Oorschot (Graduate Student Member, IEEE) was born in Lewedorp, The Netherlands, in 1994. He received the M.Sc. degree in electrical engineering from the Eindhoven University of Technology (TU/e), Eindhoven, The Netherlands, in 2019. His master's thesis was on the design of a short rise time solid-state high-voltage pulse generator.

In September 2019, he joined the Electrical Energy Systems Group, TU/e, as a Ph.D. Researcher, where his work focuses on the design of flexible, solid-state pulse generators for plasma-activated water generation.

T. Huiskamp (Member, IEEE) was born in Den Dolder, The Netherlands, in 1985. He received the M.Sc. and Ph.D. degrees (Hons.) in electrical engineering from the Eindhoven University of Technology (TU/e), Eindhoven, The Netherlands, in 2011 and 2015, respectively.

He worked as a Visiting Researcher with Kumamoto University, Kumamoto, Japan; the University of Southern California, Los Angeles, CA, USA; and the Leibniz Institute for Plasma Science and Technology (INP Greifswald), Greifswald, Germany. As a Ph.D. Researcher, he worked on nanosecond pulsed power-induced corona plasmas with the Electrical Energy Systems Group, TU/e, where he is currently an Assistant Professor. His main area of expertise is flexible, adjustable parameter (sub)nanosecond pulse source development and their application to transient plasmas for air purification and plasma-activated water generation applications.